

# **IEICE** **TRANSACTIONS**

## **on Communications**

DOI:10.23919/transcom.2024EBP3146

This advance publication article will be replaced by the finalized version after proofreading.

**A PUBLICATION OF THE COMMUNICATIONS SOCIETY**



The Institute of Electronics, Information and Communication Engineers  
Kikai-Shinko-Kaikan Bldg., 5-8, Shibakoen 3chome, Minato-ku, TOKYO, 105-0011 JAPAN

## PAPER

# Frequency Sinogram Based Cancer Recognition via Convolutional Neural Network for Microwave Breast Cancer Diagnosis

Ayumi UEDA<sup>†</sup>, *Student Member* and Shouhei KIDERA<sup>†a)</sup>, *Senior Member*

**SUMMARY** In this paper, we present a frequency sinogram data-based cancer recognition model employing a convolutional neural network (CNN) scheme for microwave-based breast cancer screening. As most cancer recognition schemes are based on radar image exploitation, these approaches have difficulty in discriminating a fibroglandular tissue from a malignant tumor, particularly in dense breasts, due to low contrast between tumor and fibro-glandular, in terms of dielectric properties. Thus, we introduce a straightforward recognition scheme involving the exploitation of a potential characteristic of backscattered frequency sinogram data. Furthermore, data augmentation schemes along an array rotation angle are introduced with a Fourier-based upsampling scheme to ensure high-accuracy recognition. The two-dimensional finite-difference time domain method using a realistic numerical phantom validates the effectiveness of our proposed approach.

**key words:** *Microwave breast cancer recognition, Convolutional neural network (CNN), Frequency sinogram data, Ultra-wideband (UWB) radar.*

## 1. Introduction

According to the World Cancer Research Fund's global statistics, breast cancer is the most frequently diagnosed fatal cancer in women [1]. The X-ray imaging modality is the most widely used screening tool; however, it involves non-negligible X-ray exposure, which harms healthy tissue and necessitates painful breast compression during measurement. Both factors contribute to a decrease in the examination rate, particularly among young women. Contrarily, low-energy microwave screening is significantly advantageous regarding safety, low cost, compactness, and non-contact measurement, which is the most critical consideration for increasing the examination rate. Furthermore, these features lead to more frequent examinations, increasing the rate of cancer detection at early stages.

Several studies and *ex vivo* investigations have demonstrated a distinct dielectric contrast between normal adipose tissue and tumor tissues [2]. This contrast aids the development of a microwave-based cancer recognition scheme, particularly for hardware designs [3–5]. There are two major approaches for implementing imaging using microwave-scattered data to identify cancerous tissue. One approach is coherent integration-based imaging, also known as confocal imaging [6–8]. However, confocal radar imaging suffers from a high false-positive rate because it offers only a qualitative spatial profile of the reflection coefficient, where

fibroglandular tissue surrounded by adipose area also generates a distinct response in the radar image. Conversely, an inverse scattering (IS) analysis, also known as the tomography approach, could provide a quantitative dielectric profile of complex permittivity by solving the domain integral equation from scattered data [9]. As the IS problem is nonlinear and generally ill-conditioned, many approaches represented by the Born approximations, the distorted Born iterative method [10, 11] or contrast source-based inversion [12, 13] have been proposed. While these methods can achieve high-accuracy cancer tissue recognition, even in highly dense breast tissue, they have an extremely high computational cost to reconstruct complex permittivity profiles, particularly in fully three-dimensional imaging scenarios. Notably, while there are many recent studies based on machine learning or deep learning (DL) schemes [14–16], each requires an appropriate imaging scheme, such as radar or tomography, to generate the input data for machine learning. Correspondingly, the recognition performance is largely dependent on the spatial resolution or reconstruction accuracy limited by the imaging condition. In particular, the reconstruction accuracy of the radar image is highly dependent on the selected propagation model, such as homogeneous assumption or a dielectric constant of the breast media, which largely varies in individuals.

To address the above problem, this study introduces a backscattered signal-based cancer recognition scheme employing a convolutional neural network (CNN) using frequency sinogram data. There are some machine learning algorithms for the binary decision of cancer existence, such as support vector machine (SVM), which is one of the nonlinear classification algorithms, however, the SVM is prone to overfitting when handling high-dimensional input data, such as time or frequency sinograms, particularly when the amount of training dataset is limited. In contrast, CNNs can significantly reduce the input-vector dimensions using convolutional processing and are suitable for high-dimensional input data. Contrary to other DL-based recognition schemes [17, 18], our scheme does not need a radar or tomographic imaging process, which often includes a non-negligible artifact, leading to a false recognition. While a similar approach to that in [19] has been introduced, it employs temporal sinogram data, which include redundant input dimensions. Moreover, its accuracy highly depends on its sampling interval or range, while an actual time delay of target response is generally unknown. Contrarily, our proposed scheme can reduce the dimension of input vectors to the

<sup>†</sup>The authors are with Graduate School of Informatics and Engineering, The University of Electro-Communications, Tokyo, Japan.

a) E-mail: kidera@uec.ac.jp\*

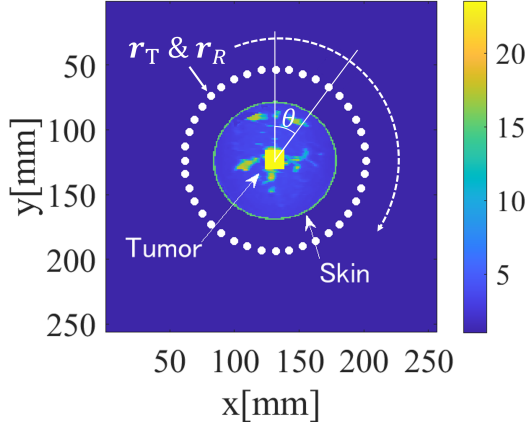


Fig. 1: Observation and breast configuration model. White dots show the sampling position of a set of transmitter and receiver (same position) at the circular curve being external at breast. The malignant tumor is located in the center of breast.

postCNN scheme by extracting complex-valued responses in a dominant frequency range. Thus, the temporal information stored in phase is preserved, and the equivalent signal-to-noise ratio (SNR) is enhanced. Additionally, by focusing on the continuity along the array rotation, the Fourier-based up-sampled circular permutation (CP) scheme is introduced to increase the volume of effective training data.

The main contributions of this study are summarized below:

1. Frequency sinogram data are directly inputted to the CNN-based cancer recognition scheme to avoid intermediate imaging process.
2. Focusing on the rotating array observation model, the up-sampled CP along the rotation axis is also introduced to remarkably increase the amount of training data.
3. Numerical tests using the MRI-derived realistic phantom demonstrate that the CP data augmentation can offer a higher recognition accuracy, and the frequency sinogram has a superiority from the temporal sinogram-based scheme, in terms of noise-robustness, particularly in a lower SNR situation.

## 2. Method

### 2.1 Observation Model

Figure. 1 illustrates the observation model. Transmitter and receiver elements are located at  $\mathbf{r}_T$  and  $\mathbf{r}_R$ , respectively, which rotate along the center of the breast.  $s(\mathbf{r}_T, \mathbf{r}_R, t, \theta)$  denotes the back-scattered signals at each combination of  $\mathbf{r}_T$  and  $\mathbf{r}_R$  with rotation angle  $\theta$ .  $s(\mathbf{r}_T, \mathbf{r}_R, t, \theta)$  includes the reflections from skin, fat, fibroglandular, and cancerous tissues, all of which have lossy and dispersive dielectric properties.

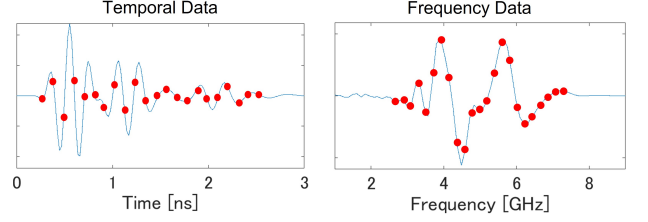


Fig. 2: Sampling examples for temporal and frequency scattered data. Red dots denote the sampling points.

### 2.2 Convolutional Neural Network (CNN) Based Recognition with Frequency Sinogram

This study introduces a cancer recognition method based on backscattered data using a supervised DL approach, specifically the CNN scheme. While numerous studies have explored DL-based cancer recognition, most of them require a preprocessing imaging scheme, such as confocal imaging. Contrarily, by focusing on a distinct feature of the DL approach, cancer recognition could be directly judged by the unprocessed backscattered datasets using multiple frequency bins. To reduce the input dimension of the post-DL process, we focus on frequency sinogram data, as follows. Here, temporal sinogram data  $\hat{s}(\mathbf{r}_T, \mathbf{r}_R, t, \theta)$  are converted into frequency sinogram data  $S(\mathbf{r}_T, \mathbf{r}_R, \omega, \theta)$  using the 1D Fourier transform along  $t$ , where the skin surface reflection is eliminated. Figure 2 illustrates the sampling examples of temporal and frequency scattered data for generating input vectors for the post DL process. When dealing with a discrete model,  $S(\mathbf{r}_i^T, \mathbf{r}_j^R, \omega_k, \theta_l)$  is defined as the scattered data assuming in the  $i$ -th transmitter,  $j$ -th receiver,  $k$ -th frequency bin, and  $l$ -th rotation angle. In this case, since we assume a single transmitter and receiver, the data  $S(\mathbf{r}_i^T, \mathbf{r}_j^R, \omega_k, \theta_l)$  data can be transformed into the 2D complex-valued input data as  $\mathbf{X}$ , in terms of the frequency  $\omega_k$  and the rotation angle  $\theta_l$  as follows:

$$X_{k,l} \equiv S(\mathbf{r}_i^T, \mathbf{r}_j^R, \omega_k; \theta_l), (k = 1, \dots, K, l = 1, \dots, L) \quad (1)$$

Thus,  $\mathbf{X} \in C^{K \times L}$  are input to the 2D CNN based classification network, where the real and imaginary parts of the complex-valued data are associated with the red and green image components of the CNN learning scheme with zero components in the blue image. Furthermore, in the training phase of the CNN, the output vector  $\mathbf{Y}$  is defined as follows:

$$\mathbf{Y} \equiv \begin{cases} 1 & (\text{w/ cancer}) \\ 0 & (\text{w/o cancer}) \end{cases} \quad (2)$$

Notably, when inputting the test data, the output vector  $\mathbf{Y}$  would take a continuous value from 0 to 1. Moreover, we set the threshold to  $\mathbf{Y}$  as 0.5 to determine whether the input vectors are assessed as a case with or without tumor, because both true positive and true negative rates are equally

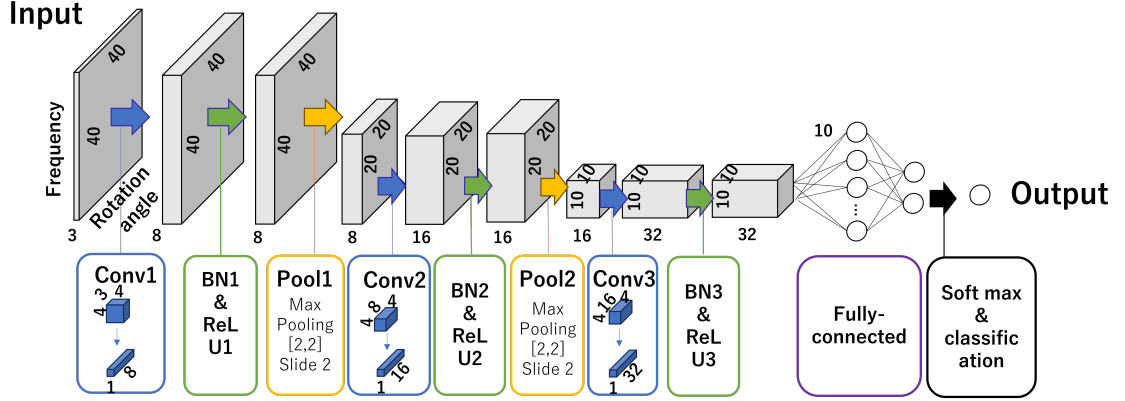


Fig. 3: The structure of the CNN and fully-connected NN model in the proposed method.

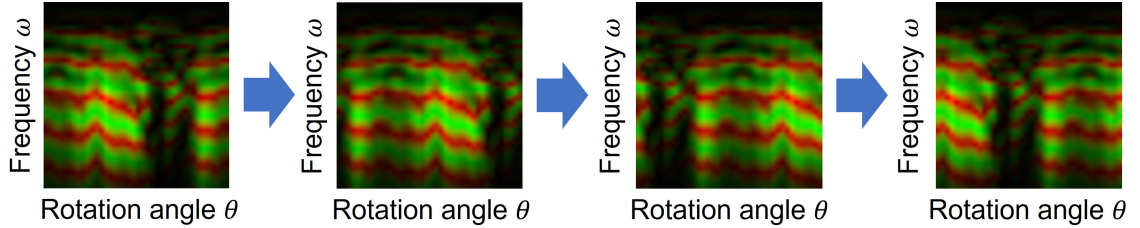


Fig. 4: Conceptual illustration of CP based data augmentation. The 2-D complex-valued input vector  $\mathbf{X}$  is converted to  $\mathbf{X}^{\text{CP}}(n)$  at each  $n$ .

important to achieve accurate cancer diagnosis. The actual configuration of the CNN is illustrated in Fig. 3.

### 2.3 Data Augmentation along Rotation Angle

Furthermore, some training data are augmented by circular permutation (CP) along rotation angle  $\theta$ . Here, the  $n$ -th CP augmented input vector  $\mathbf{X}^{\text{CP}}(n) \in C^{K \times L}$  is denoted as:

$$X_{k,l}^{\text{CP}}(n) \equiv X_{k,l'(n)} \quad (3)$$

$$l'(n) \equiv (l + n) \bmod L, (n = 1, \dots, N) \quad (4)$$

where  $\bmod L$  denotes the modulo operator with  $L$ . We call this data augmentation process as CP in the following evaluation. Figure 4 shows the conceptual illustration denoting the principle of CP based data augmentation. Notably, while the size of input vector  $X_{k,l}^{\text{CP}}(n)$  is the same as that of  $\mathbf{X} \in C^{K \times L}$ , the number of training samples becomes the  $N$ -times larger than that when the CP process is not employed, which helps avoid an over-fitting in the optimization process.

## 3. Results: Numerical Test

### 3.1 Numerical Setup

Here, the dispersive finite-difference time domain (FDTD) method (cell size: 1 mm) is employed to generate scattered

data. A single set of transmitter and receiver elements is rotated  $360^\circ$  with 40 samples, as shown in Figure 1. The transmitted current forms a 5.06 GHz center and 3.45 GHz bandwidth, which are approximately the same as those for the actual UWB radar module in [5]. The frequency-dependent dielectric properties of each breast tissue are modeled using single-pole Debye models as  $\tilde{\epsilon}(\omega) = \epsilon_\infty + \frac{\epsilon_s - \epsilon_\infty}{1 + j\omega\tau_0} + \frac{\sigma}{j\omega\epsilon_0}$  over the frequency range from 0.1 GHz to 5.5 GHz, as described in [2]. Here, as the MRI-derived numerical phantom of healthy women, a Class-2 ‘‘Scattered Fibroglandular’’ breast phantom is used, as one of the most representative categories among other classes, which is available from an online repository in [21]. As many investigations suggested, a cancerous tissue has 1.2 times greater complex permittivity than the highest value of fibroglandular tissue, which is located in the center of the breast, with a size of  $15 \text{ mm}^2$ . Twenty different cross-sectional patterns are extracted from the Class 2 phantom to generate the training and test data sets. Notably, each pattern includes or does not include a cancer cell in the center of the breast, that is, total 40 patterns are investigated as presented in Fig. 5. The sampling number of the rotation angle is 40 ( $L = 40$ ), denoting 9 degree spacing, from 0 degree to 351 degree. Moreover, both the sampling number of the frequency or temporal data is set to 40 ( $K = 40$ ), and the range of each sampling is summarized in Table 1. A perfect rejection of skin reflection is assumed, for simplicity. The parameters in the CNN and fully connected multi-layer perceptron (FC-MLP) structure

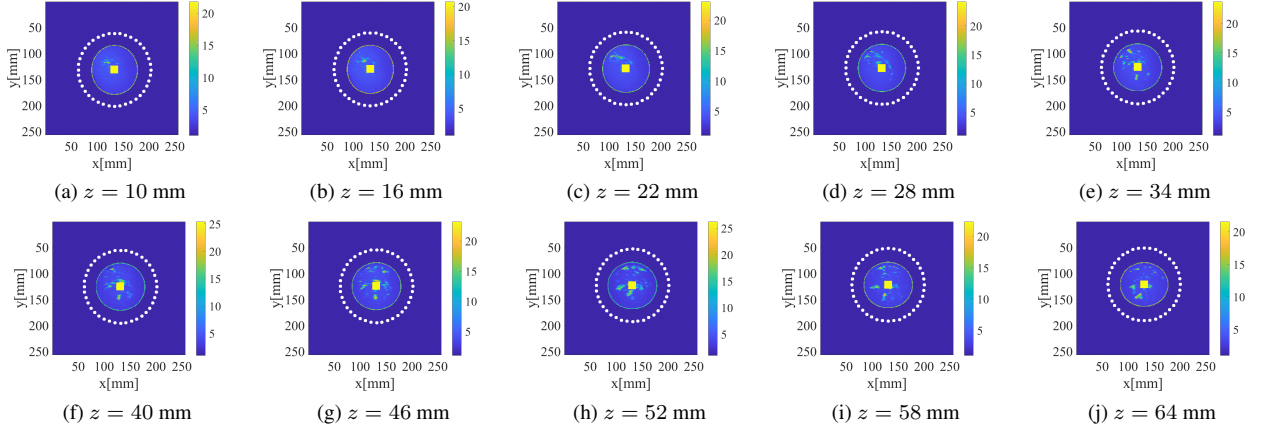


Fig. 5: Data sets: Spatial profiles of Debye parameter  $\epsilon_{\infty}$  at the different cross-sectional image in Class 2.

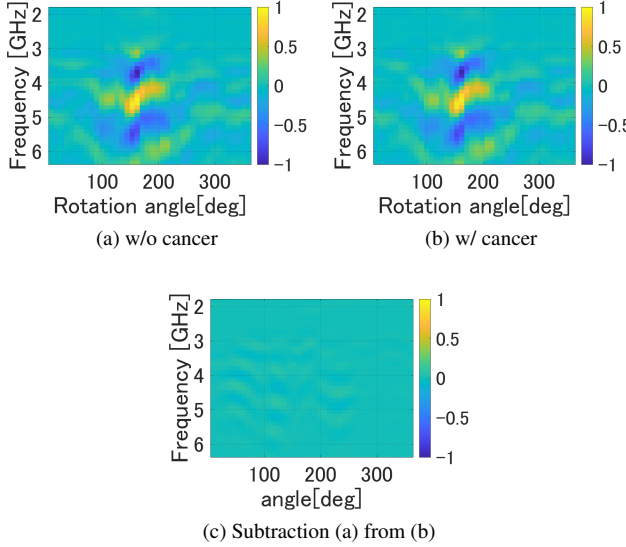


Fig. 6: Examples of the frequency sinogram data with and without cancer tissue. (c) denotes the subtraction (a) from (b), denoting only the response of cancer tissue.

Table 1: Sampling number and spacing in frequency and temporal sinogram data.

	Range	Spacing
Temporal	[0.085ns, 3.397ns]	0.085 ns
Frequency	[1.840GHz, 6.326GHz]	0.115 GHz

as shown in Fig. 3. is summarized in Table 2.

### 3.2 Recognition Results

At first, Fig. 6 shows an example of frequency sinograms ( $|S(\mathbf{r}_i^T, \mathbf{r}_j^R, \omega_k, \theta_l)|$ ) with and without cancer tissues, for the cross-sectional pattern at  $z = 3$  mm, which are inputted into the CNN learning process. Fig. 6-(c) shows the subtraction signal of the scattered data between with and without a cancer case; that is, it only expresses a cancer response. As illustrated in Fig. 6-(c), the cancer response is considerably

Table 2: Parameters in the CNN. SGDM stands for stochastic gradient descent with a momentum.

Number of Convolutional layers	3
Number of neuron in FC-MLP	(10,2)
Rate of Validation Data	0.1
Optimization algorithm	SGDM
Initial learning rate	0.01

weaker than those of other clutters, *e.g.*, scattered fibroglandular tissue, even in complete suppression from skin reflection, and its maximum response is approximately -20 dB from that of the clutters. In other words, it is highly difficult to discriminate cancer tissue from scattered fibroglandular tissues only using scattered sinogram data.

Fig. 7-shows the boxplots of recognition accuracies using frequency and temporal sinograms, with or without the CR based data augmentation, where the "CP ( $N$ )" denotes that the data augmentation rate is set to  $N$  in Eq. (4). Notably, for  $N = 120$  or  $N = 160$ , we apply the Fourier based interpolation processing along the rotation angle to decrease the sampling interval of the rotation angle. Here, the leave-one-out scheme is introduced to evaluate the recognition accuracy (the average of true positive and true negative rates) for 40 patterns, where a 10 % validation split is also introduced in the training phase. Since the CNN optimization result is randomly changed by a random optimization scheme, the 50 trials in the CNN optimizations are performed, and their accuracies are averaged over the trial number (50).

The results in Fig. 7 show that the CP based data augmentation approach can retain higher recognition accuracy in both the frequency and temporal sinograms data exploitation. This is because by increasing the amount of training data along the rotation axis, the ambiguity of the differences between the rotation angle and the existence of cancer cells can be resolved. Notably, no significant differences are observed by increasing  $N$  in the CP processing, because the increase in  $N$  corresponds to the up-sampling process, which interpolates the time or frequency data along the rotation angle,  $\theta$ , and primarily augment the dataset with similar information to the case of  $N = 40$  (CP (40)). On the other

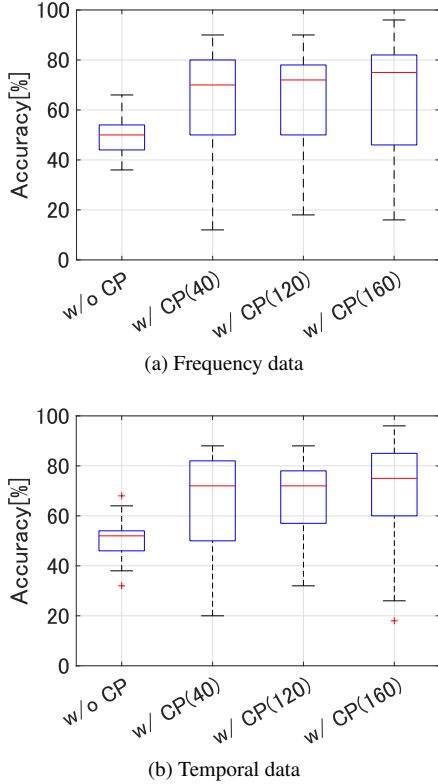


Fig. 7: Boxplot of accuracy for without or with CR process, where the number of samples  $N$  is changed.

hand, the CP process inherently increases the amount of independent data along the rotation axis, and this leads to a distinct improvement in recognition accuracy compared to the case without using the CP processing as shown in Fig. 7. To discuss in the statistically quantitative analysis for these results, Tables 3 and 4 present the  $p$ -values in two-sample  $t$ -tests among possible combinations of "w/o CP", "w/ CP (40)", "w/ CP (120)", and "w/ CP (160)". These tables demonstrates the significant statistical superiority achieved by using the CP process, where all the  $p$ -values are less than 0.05. Furthermore, while there are small variability among the results in "w/ CP (40)", "w/ CP (120)", and "w/ CP (160)" in Fig. 7 due to the different number of training, the  $p$ -values ( $> 0.1$ ) shown in Tables 4 and 3 indicate no statistically difference among these results. Additionally, regarding the sampling number  $L$  of the rotation angle, a certain number of samples would be required to obtain significant responses from internal tissues, such as cancer or fibro-glandular, which may vary depending on the observation angle. In contrast, when  $L$  increases, it generates higher dimension data as input vectors, resulting in over-fitting issue during the learning process. Therefore, in this study, we empirically selected  $L = 40$  to balance the number of input dimensions and the above-mentioned variations along the rotation angle.

Furthermore, to reveal the relationship between accuracy and the density of the breast, *i.e.*, the dominant ratio

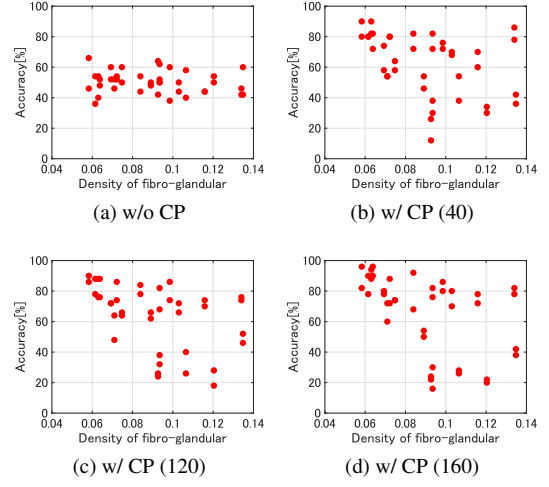


Fig. 8: Scattered plot between recognition accuracy and density of breast using frequency sinogram based CNN.

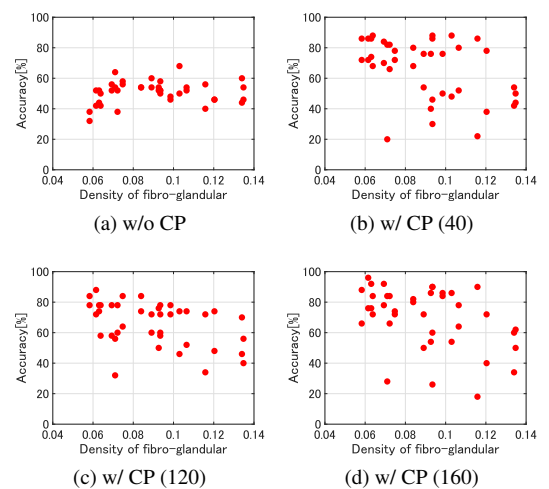


Fig. 9: Scattered plot between recognition accuracy and density of breast using temporal sinogram based CNN.

of fibroglandular tissues, Figures 8 and 9 show the scattered plots of the accuracy against the density of fibro-glandular tissues. Table 5 also presents the correlation coefficient between the accuracy and the density of the fibro-glandular tissues. These figures indicate that there is a significant negative correlation between the fibroglandular density and the recognition accuracy, in using any CR process (Fig. 8-(b), (c), and (d). Fig. 9-(b), (c), and (d).) These results clearly indicate that clutter responses from fibroglandular tissues would significantly affect the recognition performance, additionally, the indicate that it is difficult to achieve high accuracy in dense breast cases, such as Classes 3 or 4. Notably, the recognition accuracy when using the CP process exhibits more variations in both the temporal and frequency sinogram cases than those without using the CP process as in Figs. 8 and 9. We consider that since the CP process can increase the number of suitable training data to avoid ambiguity in the rotation angle, it retains a more accurate recogni-

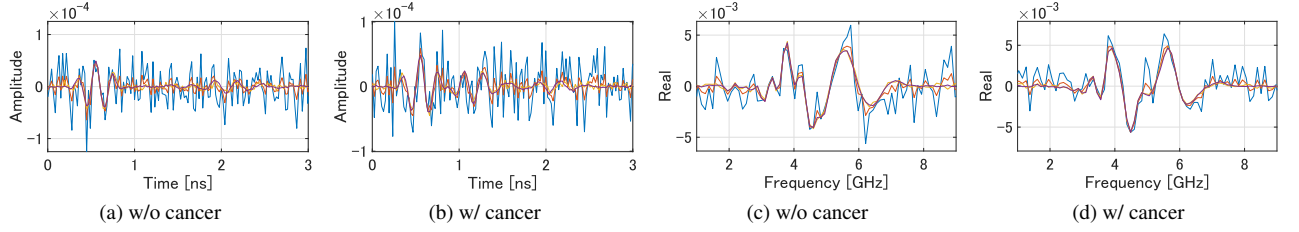


Fig. 10: Scattered responses in each SNR level. (a) and (b) : Temporal response. (c) and (d) : Frequency response. Blue line: SNR = -10 dB. Red line : SNR = 0 dB. Cyan : SNR = 10 dB. Black : SNR =  $\infty$ .

Table 3:  $p$ -values in two-sample  $t$ -test in using frequency sinogram data. The hypothesis is "row  $\geq$  column".

	w/ CP (40)	w/ CP (120)	w/ CP (160)
w/o CP	$2.36 \times 10^{-4}$	$5.71 \times 10^{-5}$	$1.71 \times 10^{-4}$
w/ CP (40)	-	0.348	0.275
w/ CP (120)	-	-	0.405

Table 4:  $p$ -values in two-sample  $t$ -test in using temporal sinogram data. The hypothesis is "row  $\geq$  column".

	w/ CP (40)	w/ CP (120)	w/ CP (160)
w/o CP	$8.33 \times 10^{-6}$	$3.14 \times 10^{-8}$	$1.01 \times 10^{-7}$
w/ CP (40)	-	0.495	0.187
w/ CP (120)	-	-	0.1588

Table 5: Correlation coefficient between accuracy and the density of fibroglandular.

	w/o CR	w/ CR		
		40	120	160
Correlation coefficient	-0.1617	-0.4135	-0.4601	-0.4917

tion performance in low-density breast tissues than in high-density breast tissues. In contrast, the recognition accuracy in high-density breast becomes lower because it is inherently challenging to extract distinct responses from cancerous tissues buried into densely distributed fibro-glandular. Using the CP processes, the above-mentioned differences can be clearly distinguished, possibly leading to more variations in the recognition accuracy.

### 3.3 Sensitivity to Additive Noise

This section describes the sensitivity study to additive noise. Here, the additive white Gaussian noise (AWGN) is added to the scattered data  $s(\mathbf{r}_T, \mathbf{r}_R, t, \theta)$  in the time domain. The signal-to-noise ratio (SNR) is defined as the ratio of the maximum signal power to the noise power, where the skin surface reflection components are completely eliminated, *i.e.*, only the scattered component from the inner tissues, *e.g.* fibro-glandular or cancer tissues. Here, we investigate the four different SNR scenarios: as -10 dB, 0 dB, 10 dB, and 20 dB. Figures 10 show the temporal and frequency responses at each SNR level. As shown in Fig. 10, particularly at SNR = -10 dB, while the temporal signal considerably suffers from a random noise component, the frequency signal

could retain a certain level of SNR, particularly around the center frequency. This is because the AWGN has a relatively wider frequency response, and the bandpass filtering effect around the available frequency range enhance the equivalent SNR. Figure 11 also shows the boxplots of the recognition accuracy at each SNR level for both the temporal and frequency sinogram approaches. This figure shows that there are no significant differences among the 20 dB, 10 dB, and 0 dB SNR levels, with or without the CR process. However, for the -10 dB SNR, the accuracy of the temporal sinogram data is considerably lower than those for the frequency sinogram, regardless of using the CR process. In addition, Table 6 and 7 present the  $p$ -values in two-sample  $t$ -tests regarding the SNR level for the frequency and temporal sinogram based approaches, respectively. While Table 6 in using the frequency sinogram, indicates that there are no significant statistical superiorities at the -10 dB SNR level compared with other higher SNR levels ( $p \geq 0.1$ ), Table 6 with the temporal sinogram, demonstrates that statistical superiority at the higher SNR is observed compared with that at -10 dB SNR level ( $p \leq 0.1$ ). Thus, these statistical analyses validate the significant advantage of the frequency sinogram-based CNN over the temporal one, regarding random noise robustness. Notably, noise robustness is one of the most critical factors to consider in practical applications because the breast media are highly lossy, and the SNR level would often be considerably low (under 0 dB). Correspondingly, our proposed scheme would be highly effective in practical applications when temporal data introduced, as in [19].

### 3.4 Further Discussions

This study investigates the numerical simulation based performance evaluation, using a realistic breast phantom, where a skin surface reflection has been completely eliminated. However, in a realistic or experimental scenario, the above skin reflection could not be completely suppressed, which incurs an incorrect identification of cancer tissue, because skin reflection is much larger than that from inner tissue. Several skin reflection suppression schemes, such as the finite-response filter [7], the two-step approach, [5] and the fractional derivative model [20], are available in the literature. Although those approaches do not require any prior knowledge of the dielectric properties of each tissue, *i.e.*, skin, adipose, or fibro-glandular, they achieve accurate skin-reflection suppression using appropriate signal processing

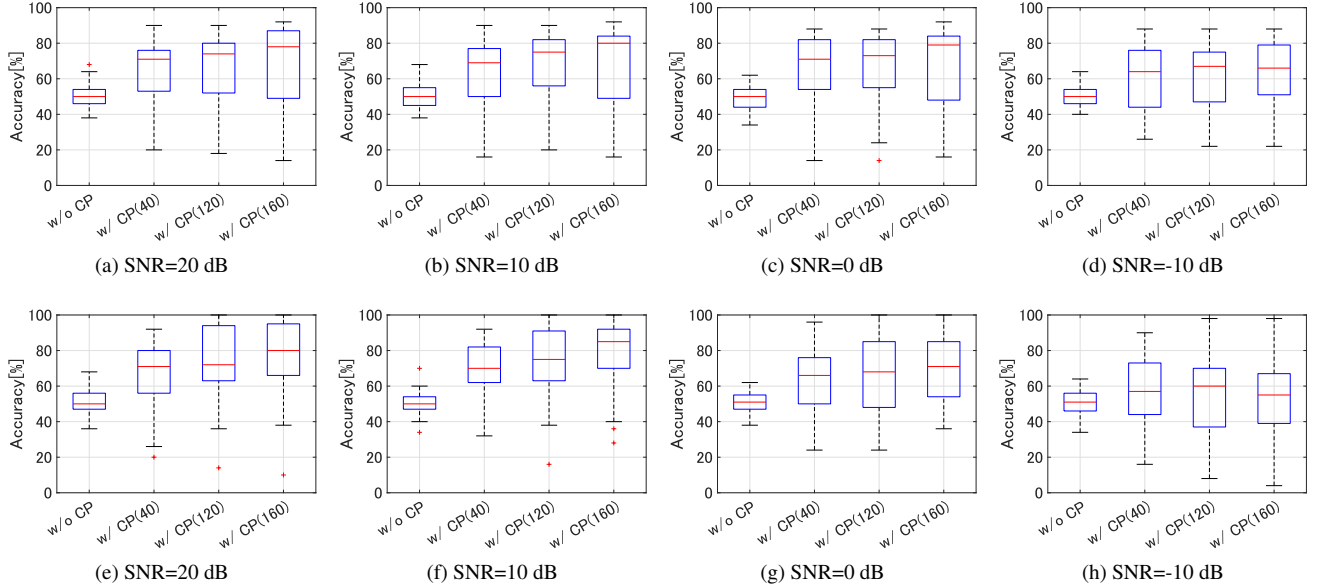


Fig. 11: Boxplot of accuracy for without or with CR process, where the number of samples  $N$  is changed in each SNR level. 1st row: Frequency data. 2nd row: Temporal data.

Table 6:  $p$ -values in two-sample  $t$ -test in terms of SNR level, in frequency data based CNN recognition at the case of w/ CP (40). The hypothesis is "row  $\geq$  column".

	0 dB	10 dB	20 dB
-10 dB	0.1753	0.2918	0.2625
0 dB	-	0.6480	0.6184
10 dB	-	-	0.4675

in conjunction with some optimization. Specifically, in our previous study [20] we introduced a fractional derivative based skin reflection suppression scheme. Notably, the skin surface reflection waveform depends on the distance between the element and the skin surface, the skin surface shape, and its dielectric property, we demonstrated that the fractional derivative based waveform model can accurately compensate for the above-mentioned waveform deformation by optimizing the parameters used for the fractional derivative, which has been validated in [20]. Thus, by combining the above scheme, our proposed scheme presented in this study can be applied in an experimental or realistic case.

In addition, while the recognition accuracy is around 80 %, there is possibility to enhance this accuracy by increasing the training data. For increasing the training data, we can also introduce the different size, shape or location of the cancer tissue, and it is our important future work. Nonetheless, in the machine learning scheme, it is important to reduce the input dimension, and our proposed scheme as frequency sinogram can effectively reduce the input dimension with enhanced SNR, compared with the existing temporal sinogram based recognition scheme.

#### 4. Conclusion

Herein, we presented a backscattered signal-based breast cancer recognition scheme using CNN learning for microwave breast cancer screening. In our method, the fre-

Table 7:  $p$ -values in two-sample  $t$ -test in terms of SNR level, in temporal data based CNN recognition at the case of w/ CP (40). The hypothesis is "row  $\geq$  column".

	0 dB	10 dB	20 dB
-10 dB	0.0581	0.0008	0.0095
0 dB	-	0.0418	0.1838
10 dB	-	-	0.7738

quency or temporal sinogram data are directly inputted to the CNN and FC-MLP neural network recognition model, which can avoid the imaging errors that limit radar or tomographic approaches. Additionally, by introducing data augmentation along the rotation axis, the proposed method retains high-accuracy recognition even with using a small amount of training data. The frequency-dependent FDTD numerical simulation, using the MRI-derived phantom, demonstrated that our CP data augmentation significantly enhanced the recognition accuracy, highly associated with the density of a fibroglandular tissue. Moreover, compared with the existing temporal sinogram approach, the frequency sinogram-based recognition offered a more noise-robust feature, attributed to the Fourier-coherent integration effect. In an ongoing study, we are investigating the application of our scheme to clinical data sets, where effective skin reflection suppression, as in [20], would be implemented to retain a high recognition accuracy.

#### Acknowledgment

This work was supported by JSPS KAKENHI Grant Number JP23K26113 and the Asahi Glass Foundation, Continuation Grants for Young Researchers.

## References

- [1] F. Bray, J. Ferlay, I. Soerjomataram, R.L. Siegel, L.A. Torre, and A. Jemal, "Global cancer statistics 2018: GLOBOCAN estimates of incidence and mortality worldwide for 36 cancers in 185 countries," *Cancer Jnl. for Clinicians*, vol.68, no.6, pp.394 – 424, Dec. 2018.
- [2] M. Lazebnik, D. Popovic, L. McCartney, *et al.*, "A large-scale study of the ultrawideband microwave dielectric properties of normal, benign and malignant breast tissues obtained from cancer surgeries," *IOP Publishing Phys. Med. Biol.* vol. 52, pp. 6093–2093 2007.
- [3] L. Kranold, M. Taherzadeh, F. Nabki, *et al.*, "Microwave Breast Screening Prototype: System Miniaturization With IC Pulse Radio," *IEEE Journal of Electromagnetics, RF and Microwaves in Medicine and Biology*, vol. 5, no. 2, pp. 168-178, June 2021
- [4] L. Fortaleza and M. Popović, "Narrowband Microwave Breast Screening: Repeatability Study With Phantoms," *IEEE Journal of Electromagnetics, RF and Microwaves in Medicine and Biology*, vol. 6, no. 2, pp. 260-266, June 2022
- [5] H. Song, S. Sasada, N. Masumoto, *et al.*, X. Xiao, and T. Kikkawa, "A Two-stage Rotational Surface Clutter Suppression Method for Microwave Breast Imaging with Multistatic Impulse-Radar Detector," *IEEE Transactions on Instrumentation and Measurement*, vol. 69, pp. 9586–9598, Jun. 2020.
- [6] D. Byrne, M. Sarafianou, I. J. Craddock, "Compound Radar Approach for Breast Imaging" , *IEEE Trans. Biomed. Eng.*, Vol. 64, no. 1, pp. 40 – 51, Jan., 2017.
- [7] E. J. Bond, Xu Li, and S. C. Hagness, "Microwave imaging via space-time beamforming for early detection of breast cancer", *IEEE Trans. Antennas Propagat.*, vol. 1, no. 8, pp. 1690-1705, Aug. 2003.
- [8] J. Moll, T. Slanina, J. Stindl, T. Maetz, D. H. Nguyen and V. Krozer, "Temperature-Induced Contrast Enhancement for Radar-Based Breast Tumor Detection at K-Band Using Tissue Mimicking Phantoms," *IEEE Journal of Electromagnetics, RF and Microwaves in Medicine and Biology*, vol. 7, no. 3, pp. 251-257, Sept. 2023
- [9] M. T. Bevacqua, S. Di Meo, L. Crocco, *et al.*, "Millimeter-Waves Breast Cancer Imaging via Inverse Scattering Techniques," *IEEE Journal of Electromagnetics, RF and Microwaves in Medicine and Biology*, vol. 5, no. 3, pp. 246-253, Sept. 2021.
- [10] W. C. Chew and Y. M. Wang, "Reconstruction of two-dimensional permittivity distribution using the distorted Born iterative method," *IEEE Trans. Med. Imag.*, vol. 9, pp. 218 - 225, June 1990.
- [11] Z. Gong, Y. Chen, Y. Ding and H. Zhang, "Perspective: Microwave Medical Imaging Using Space-Time-Frequency A Priori Knowledge for Health Monitoring," *IEEE Journal of Electromagnetics, RF and Microwaves in Medicine and Biology*, vol. 8, no. 1, pp. 2-14, March 2024
- [12] P. M. van den Berg and A. Abubakar, "Contrast Source Inversion Method: State of Art," *Progress In Electromagnetics Research, PIER 34*, 2001, pp. 189–218.
- [13] H. Sato and S. Kidera, "Noise-robust Microwave Breast Imaging Applied to Multi-frequency Contrast Source Inversion", *IEEE Journal of Electromagnetics, RF, and Microwaves in Medicine and Biology*, 2021.
- [14] L. Li, L. G. Wang, F. L. Teixeira, *et al.*, "DeepNIS: Deep Neural Network for Nonlinear Electromagnetic Inverse Scattering," *IEEE Trans. Antennas & Propagation*, vol. 67, no. 3, pp. 1819-1825, March 2019.
- [15] Y. Zhou, Y. Zhong, Z. Wei, *et al.*, "An Improved Deep Learning Scheme for Solving 2D and 3D Inverse Scattering Problems," *IEEE Transactions on Antennas and Propagation*, 2020.
- [16] Z. Wei and X. Chen, "Physics-Inspired Convolutional Neural Network for Solving Full-Wave Inverse Scattering Problems," *IEEE Transactions on Antennas and Propagation*, vol. 67, no. 9, pp. 6138-6148, Sept. 2019.
- [17] N. Khalid, M. Hashir, N. Mahmood, *et al.*, "Efficient Deep Learning Approaches for Automated Tumor Detection, Classification, and Localization in Experimental Microwave Breast Imaging Data," *2023 IEEE International Symposium on Circuits and Systems (IS-CAS)*, Monterey, CA, USA, 2023, pp. 1-4.
- [18] S. Costanzo, A. Flores and G. Buonanno, "Fast and Accurate CNN-Based Machine Learning Approach for Microwave Medical Imaging in Cancer Detection," in *IEEE Access*, vol. 11, pp. 66063-66075, 2023.
- [19] T. Reimer and S. Pistorius, "The Diagnostic Performance of Machine Learning in Breast Microwave Sensing on an Experimental Dataset," *IEEE J. Electromagn. RF Microw. Med. Biol.*, vol. 6, no. 1, pp. 139-145, Mar. 2022.
- [20] K. Noritake, S. Kidera, "Surface Clutter Suppression with FDTD Recovery Signal for Microwave UWB Mammography", *IEICE Trans. Electron.*, vol. E103-C, No.1 Jan., 2020.
- [21] UWCEM, "Numerical breast phantom repository", URL:<https://uwcem.ece.wisc.edu/phantomRepository.html>

**Ayumi Ueda** received the B.E. degree in communication engineering and informatics from the University of Electro-Communications, Tokyo, Japan, in 2023. She is currently pursuing the M.E. degree with the Graduate School of Informatics and Engineering in the University of Electro-Communications, Tokyo, Japan. Her research interest includes signal processing, imaging, and deep learning approaches for microwave biomedical applications.

**Shouhei Kidera** received his B.E. degree in Electrical and Electronic Engineering from Kyoto University in 2003 and M.I. and Ph.D. degrees in Informatics from Kyoto University, Kyoto, Japan, in 2005 and 2007, respectively. In 2009, he joined as an Assistant Professor with the University of Electro-Communications, Tokyo, Japan, where he is currently a full Professor with Graduate School of Informatics and Engineering in the University of Electro-Communications, Tokyo, Japan.

His current research interest is in advanced radar signal processing or electromagnetic inverse scattering issue for ultra wideband (UWB) three-dimensional sensor or bio-medical applications. He has been stayed at the Cross-Disciplinary Electromagnetics Laboratory in the University of Wisconsin Madison as the visiting researcher in 2016. He has been a Principal Investigator of the PRESTO Program of Japan Science and Technology Agency (JST) from 2017 to 2021. He was a recipient of the 2012 Ando Incentive Prize for the Study of Electronics, 2013 Young Scientist's Prize by the Japanese Minister of Education, Culture, Sports, Science and Technology (MEXT), and 2014 Funai Achievement Award, 2022 KDDI Foundation Award, Contribution Award, and 2023 RIEC Award. He is a senior member of the Institute of Electrical and Electronics Engineering (IEEE), and a member of the Institute of Electrical Engineering of Japan (IEEJ), and the Japan Society of Applied Physics (JSAP).